Journal of Petroleum Science and Engineering 175 (2019) 961–970

Contents lists available at ScienceDirect

Journal of Petroleum Science and Engineering

journal homepage: www.elsevier.com/locate/petrol

Micro-scale investigation on coupling of gas diffusion and mechanical deformation of shale

Mingyao Wei[a,b,*], Yingke Liu[c,d], Jishan Liu[e], Derek Elsworth[f], Fubao Zhou[c,d]

[a] IoT Perception Mine Research Center, China University of Mining & Technology, Xuzhou, Jiangsu, 221116, China
[b] State Key Laboratory of Geomechanics and Geotechnical Engineering, Institute of Rock and Soil Mechanics, Chinese Academy of Sciences, Wuhan, 430071, China
[c] Faculty of Safety Engineering, China University of Mining & Technology, Xuzhou, Jiangsu, 221116, China
[d] Key Laboratory of Gas and Fire Control for Coal Mines (Ministry of Education), China University of Mining & Technology, Xuzhou, Jiangsu, 221116, China
[e] Department of Chemical Engineering, School of Engineering, The University of Western Australia, 35 Stirling Highway, Perth, WA, 6009, Australia
[f] Department of Energy and Mineral Engineering, G3 Center and Energy Institute, The Pennsylvania State University, University Park, PA, 16802, USA

ARTICLE INFO

Keywords:
Nanopores
Micro-scale
Explicit simulation approach
Diffusion coefficient

ABSTRACT

The nanopore structure usually exhibit complex geometry in the shale formation. The interactions between gas and pore structure in such heterogeneous property impacts the properties of shale gas transport in micro-scale. The precise description of this shale gas flow processes in detail is impossible if the micropore is not properly characterized. Thus, this study provides a simulation approach to model the complex geometry of nanopore structures in the shale formation. Based on SEM image segmentation of the shale matrix, the geometry of three compositions (nanopore, kerogen, and matrix) are explicitly simulated. Mass storage, transport mechanisms, and geomechanical properties are fully modeled in the micro-scale model. It demonstrates that the conventional dual porosity model fails to capture the storage and transport mechanisms in micro-scale by comparison with the micro-scale model. The simulation results reveal that stress-induced decrease of the diffusion coefficient is both time-dependent and space-dependent. The reduction of the diffusion coefficient can significantly cut down the adsorbed gas production in kerogen. It results in the low recovery rate of shale gas that a large proportion of adsorbed gas is unable to liberate. Moreover, the later stage of gas production is depended on the supply of adsorbed gas in kerogen.

1. Introduction

Shale gas reservoir is a typical unconventional hydrocarbon resource, which is characterized by nanopores in tight matrix with ultra-low permeability. In shale resources, large portions of the initial gas in place is stored within the micro-scale pores of kerogen (Wei et al., 2018). Understanding the complex micro-scale transport mechanisms have great significance for accurate predictions and improvement of recovery rates of shale gas reservoir.

Recent high resolution imaging of shale matrix produced by scanning electron microscopy (SEM) have shown that pores consist of organic matter pores, interparticle pores, and intraparticle pores with sizes range from nanometer to micrometer (Curtis et al., 2011; Loucks et al., 2015; Mehmani et al., 2013). It is generally believed that the reservoir matrix is commonly composed of clay/silica, organic matter/kerogen and some minerals primarily (Wei et al., 2018). Thus the shale reservoir can be described as four categories, such as organic porosity, inorganic porosity, natural fractures and hydraulic fractures (Yan et al., 2013). The organic-matter fragments, as the scattered porous medium, is distributed in the shale matrix. Reed et al. (2007) evaluates that organic-matter porosity ranges from 0 to 25%. Both of adsorbed gas and free gas stored in organic matter. Free gas transfers in organic matter through the nanopores (Wang and Reed, 2009). The other part of free gas in shale is stored in the natural fractures and micro-pores of the matrix system. The pore space hosts free gas and adsorb gas at the same time because of large internal surface areas. Note that the amount of gas adsorbed on the inorganic walls is considered inappreciable compared to adsorbed gas in kerogen.

Many continuum approaches have been developed on the basis of single-porosity or dual-continuum models for describing of the fluid flow in unconventional reservoirs (Barenblatt et al., 1960; Ertekin et al., 1986; Cipolla et al., 2010). It provide a simpler alternative in which the dual porosity geo-material is described as a single homogeneous medium. It accurately capture the bulk properties of the shale that are suitable for the homogenization process. The advantage to equivalent continuum model is that it reducing the input data requirements,

* Corresponding author. IoT Perception Mine Research Center, China University of Mining & Technology, Xuzhou, Jiangsu, 221116, China.
E-mail address: mywei@whrsm.ac.cn (M. Wei).

https://doi.org/10.1016/j.petrol.2019.01.039
Received 22 August 2018; Received in revised form 31 October 2018; Accepted 7 January 2019
Available online 11 January 2019
0920-4105/

theoretical complexity, and computational cost (Hosking et al., 2017). However, the dual-porosity models are limited for the assumption of uniform matrix-block sizes and geometries throughout the reservoir which is too simplistic for actual shale reservoirs (Alahmadi, 2010). It appears that the dual-continuum models too regular to characterize the distribution of each continuum and the connections between those continua for shale reservoirs (Yan et al., 2016). The accuracy of equivalent continuum model for shale is low because of the ultra-low formation permeability, large matrix block and the non-linear pressure distribution in the matrix grid (Farah, 2017).

Clearly, there remains strong concern for accurately prediction of gas production from unconventional reservoirs with suitable model (Yan et al., 2016). The detailed physics of the transport process and the interaction between two different porosities need be included. Si et al. (2018) explore the influence of pore geometry structure on the gas permeability. The results imply that pore geometry structures cannot be ignored. Wua et al. (2015) described gas transport in organic nanopores of shale gas reservoirs. The stress dependence of the nanopore radius is described with an exponential equation. Janiga et al. (2018) proposed a methodology that laboratory experiments were conjuncted with the numerical representation of a core sample to generate trustworthy models. Yan et al. (2016) consider that conventional dual-porosity/permeability models are fail to characterize those complex physics and dynamics. They establish a micro-scale model for shale based on the reconstructed pores distribution. This model is able to capture multiple pore scales and flow mechanisms. However, the reconstruction methods neglect the details of particle geometry and parameters are not easily acquired (He et al., 2015). Currently, it is able to visualize the pore structures at the micro-scale using the imaging technology. The method of digital rock reconstruction attempts to build more realistic structures with geometric details through enhancement in microscope instrumentation and in image mapping technology. The accuracy of this method totally dependents on the image resolution of pore structure. Besides, it needs high-performance computing and huge storage space for data (Al-Owihan et al., 2014; Amabeoku et al., 2013; Walls, 2012).

Gas transport in shale gas reservoirs is a multiple mechanism coupling process as a result of heterogeneity and multiscale pore size, which is unlike conventional reservoirs. Meanwhile, due to the extremely low permeability in unconventional reservoirs, traditional Darcy law equation cannot be used to interpret gas flow in the shale formation. Because the complexity of pore size characterization, the gas flow in the shale matrix should be described by multi-mechanisms. Transport of free gas in nanopores and surface diffusion of adsorbed gas exist at the same in shale gas reservoirs (Akkutlu and Fathi, 2012). Knudsen number (Kn) is used to identify the transport mechanism. Currently, many researchers investigate the free gas transport mechanisms in shale include continuous flow, slip flow and transition flow (Fathi and Akkutlu, 2014; Hadjiconstantinou, 2006; Javadpour, 2009; Karniadakis et al., 2004; Moghanloo and Javadpour, 2014). The concept of apparent permeability taking into account Knudsen diffusion, gas slippage, and advection flow was derived (Clarkson and Ertekin, 2010; Ertekin et al., 1986; Javadpour, 2009), and it was further applied to pore-scale modeling for shale gas (Ali Beskok, 1999; Shabro et al., 2011). It was applied to modeling shale-gas at pore scale by Shabro et al. (2011). Civan (2010) and Ziarani and Aguilera (Ziarani and Aguilera, 2012) proposed an approach to estimate apparent permeability through the flow condition function (a function of Knudsen number) and the intrinsic permeability of porous medium. Mehmani et al. (2013) present a pore network model to determine the permeability of shale gas matrix considering the pressure induced permeability change. It characterizes gas flow in multi-scale pores range from nanometer and micrometer sizes by modeling different flow physics mechanisms.

Stress dependence causes to decrease gas transport due to the decrease of pore radius (Wua et al., 2015). During depressurization development in shale gas reservoirs, the effective stress enhances, inducing matrix particles rearrangement and crushing (David et al., 1994). The stress-sensitivity of shale occurs with specific petrophysics phenomenon, such as a dramatic decline of the pore size, porosity, and intrinsic permeability. Experimental results (Dong et al., 2010; Mckernan et al., 2014) showed that permeability may decreases by two orders of magnitude when the effective stress increases in shale experiments. The permeability of silty-shale was one to two orders of magnitude smaller when confining pressure increases from 3 MPa to 10 MPa (Dong et al., 2010). The permeability measured parallel to the layering reduced by 2–3 orders of magnitude when effective stress was increased from 10 to 70 MPa. The sample perpendicular to layering experienced a slightly smaller decrease in permeability (Mckernan et al., 2014). A stress dependence effect, giving rise to the changing petrophysical properties, does not only influences gas transport behavior, but also influence the pressure distribution in shale gas reservoirs. A lot of theories have been proposed to describe the influence of stress sensitivity, matrix shrinkage and adsorption layer on shale gas permeability in macro-scale (Durucan and Edwards, 1986; Harpalani and Schraufnagel, 1990; Shi and Durucan, 2004; Robertson and Christiansen, 2006; Palmer, 2009; Pan et al., 2010; Liu et al., 2011; Wei et al., 2016a,b; Janiga et al., 2017). However, there are few studies focused on the gas diffusion under the influence of interactions between gas and shale structure in micro-scale.

The nanopore structures usually exhibit complex geometry in the shale formation. The pores in micro-scale are important for gas storage and transport. The interactions between gas and pore structure in such heterogeneous property have an impact on the characteristics of shale gas transport in micro-scale. The precise description of the shale gas flow processes in detail is impossible if the micropore is not properly characterized and the storage and transport mechanisms are not accurately identified (Mehrabi et al., 2017). Therefore, understanding shale gas mass transfer through these nanopores is essential for understanding the overall shale gas production mechanisms. Thus, we proposed an approach to simulate gas transport and storage behavior in nanopores with the explicit discretization of pore geometry based on SEM image. This model takes complex nanopore structures into consideration. The coupling process of gas diffusion and mechanical deformation is modeled. And their effect on actual gas production is discussed.

2. Modeling of gas flow in micro-scale considering stress influence

2.1. Mass balance equation for gas flow in micro-scale matrix block

The shale gas reservoir has a wide pore size distribution from nanometers to micrometers. The matrix is the main storage space of shale gas. Characteristics of the nano-scale pore are crucial in assessing the resource potential of gas shale. The pore structures in shale are varied and heterogeneous (Bernard et al., 2012; Bustin et al., 2008). The SEM images show that the matrix block of shale is composed of two distinct parts, organic and inorganic. The organic material is primarily comprised of kerogen material, a mixture of organic chemical compounds insoluble in common polar solvents such as chloroform or dichloromethane (Tissot and Welte, 1984). Kerogen is the predominant part of organic matter in most shales (Vandenbroucke and Largeau, 2007). Thus, kerogen is a key component of shale and plays an important role in the storage and recovery of shale gas. Hashmy et al. (2011) claim that the porosity inside the kerogen can reach up to 40%. Kerogen can be further divided into two parts, porous structure (nanopores) and kerogen bulk (solid). The inorganic matter contains clay, calcite, quartz, carbonates and so on. Nanopores in both organic and inorganic regions dominate the shale gas reservoir pore structure. As can be seen from the sections in Fig. 1, almost all the large pores are exclusively located inside the kerogen. There are also some pores in the kerogen and matrix, which are much smaller. In shale formations, shale gas, in general, is stored as free gas and adsorbed gas. The free gas is

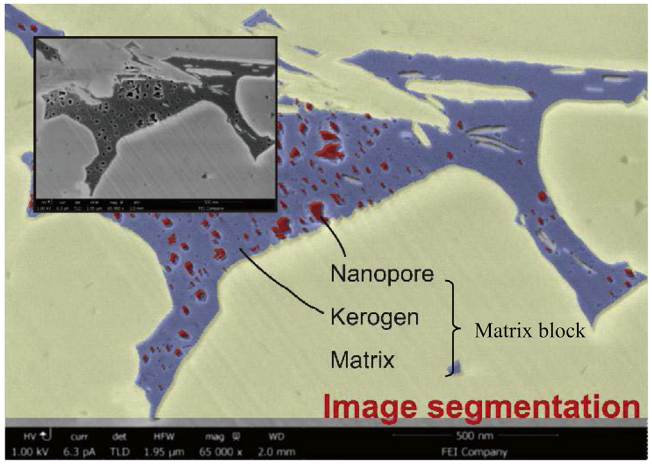

Fig. 1. SEM image segmentation of a matrix block (After Rodriguez et al., 2014). Red zone represents nanopore; Blue zone represents kerogen; Yellow zone represents matrix. (For interpretation of the references to color in this figure legend, the reader is referred to the Web version of this article.)

stored in the fractures and pores space of a mineral matrix. Adsorbed gas gathers on the inner surfaces of nanopores in kerogen. Generally, with higher content of kerogen, the sorption of hydrocarbon is higher. (Reed et al., 2007).

In order to characterize the mass transport and geomechanical properties of shale in the micro-scale, the microstructure of shale matrix based on SEM image was investigated firstly. The SEM image is a grayscale image where the pixel value varies from 0 to 255 denoting the different shades of gray. It produces a high-resolution planar image of the sample surface. Thus, higher-resolution SEM images provide information on pore structure, pore size, surface topography and composition of a shale on micrometer to nanometer scale (Bonnie and Fens, 1992). Fig. 1 shows that the shale consists of nanopores, kerogen and shale matrix with different grey levels. Image segmentation can be used to separate pores at different scales (Suri, 2011). The shale matrix bulk is strictly separated into the matrix (inorganic matrix) and kerogen (organic matrix). Two types of porosity system in kerogen is distinguished to emphasize the organic matter in the shale matrix. One kind pore is nanopores with visible pore space. The other part is kerogen matter with pores unable to distinguish in the image. In order to better divide the fractures and matrix, between-class variance maximization algorithm was selected to make the image segmentation process accurately (Baradez et al., 2004). The noises in the images were firstly suppressed to perform better image segmentation. We select the median filtration method to smooth the boundary (Gallagher and Wise, 1981). The greyscale threshold values were assigned visually for nanopore, kerogen, and matrix respectively. Based on the greyscale thresholds, the region of interest can be extracted from the unnecessary region. The segmented compositions of matrix block are shown in Fig. 1. The red zone represents the nanopores with an average radius of 30 nm embedded in the kerogen. The kerogen is represented by blue zone and the rest of zone is an inorganic matrix with marked with yellow color. It is obvious that kerogen containing tiny pores is much permeable than tight shale matrix.

The balance equations for gas transport and mechanical behavior on the microscale was established based on the principle of conservation of mass. The temporal derivative of the gas content is equal to the spatial gradient of the relevant fluxes. Sink source terms are included allowing for mass exchange between the different continua. The constitutive mass balance equation on gas in shale is given by:

$$\frac{\partial m_a}{\partial t} - \nabla \cdot J = Q \tag{1}$$

Gas adsorption in shale can be adequately described by Langmuir (1918) adsorption model despite the heterogeneity of the gas adsorption sites in shale. Compared with the physical process of surface diffusion, gas desorption is a quick process during depressurization of shale gas reservoirs. Hence, the total amount of adsorbed gas and free gas can be calculated as (Wei et al., 2016a,b):

$$m_a = (1-\phi)\rho_s \rho_a \frac{L_a p}{p + L_b} + \phi p \frac{M}{RT} \tag{2}$$

where ϕ is porosity of kerogen in shale, ρ_s is shale density, ρ_a is gas density at atmospheric pressure in kerogen system, L_a represents the Langmuir volume constant, L_b represents the Langmuir pressure.

The important feature of shale is the nanoscale size of pores, in both organic and inorganic matters. Due to the nanoscale pores in shale, diffusion plays an important role. Two major mechanisms contribute to the gas flow in a single, straight, cylindrical nanotube (Javadpour, 2009). The total mass flux of a gas through a nanopore is the result of a combination of Knudsen diffusion and pressure forces,

$$J = J_a + J_D \tag{3}$$

where J is the total mass flux. The first term on the right-side is advective flow due to pressure forces; the second term is Knudsen diffusion.

The nanopores in shale composite of the gas diffusion channel. The nanopores are assumed as a bundle of nanochannels. Mass flux for an ideal gas in laminar flow in a circular tube with a negligible length of entrance effect can be derived from Hagen-Poiseuille's equation as (Bird et al., 2007):

$$J_a = -\frac{\rho r^2}{8\mu}\nabla p \tag{4}$$

where r is the pore radius, ρ is the gas density, u is the gas viscosity.

Roy et al. (2003) showed that Knudsen diffusion in nanopores can be written in the form of the pressure gradient. Gas mass flux by diffusion with negligible viscous effects in a nanopore is described as (Javadpour, 2009; Roy et al., 2003):

$$J_D = -\frac{MD}{RT}\nabla p \tag{5}$$

$$D = \frac{2r\phi}{3\tau}\sqrt{\frac{8RT}{\pi M}} \tag{6}$$

where M is the molar mass, D is the diffusion coefficient for shale, R is the gas constant and T is the absolute temperature in Kelvin, τ is the tortuosity factor of nanopore.

Combining Eqs. (3)–(6), yields the total mass flux as:

$$J = -\frac{\rho r^2}{8\mu}\nabla p - \frac{M\phi}{RT\tau}\frac{2r}{3}\sqrt{\frac{8RT}{\pi M}}\nabla p \tag{7}$$

It is evident that the mass flux is related to pore size. The pore space is sensitive to change in stress or pore pressure. It implies that pore size is stress-dependent. According to our previous work on the effective strain-based absolute porosity model (Liu et al., 2011; Wei et al., 2016a,b), we can obtain:

$$\frac{\Delta V_p}{V_p} = -\frac{\alpha}{\phi K}(\Delta\sigma - \Delta p) + \Delta\varepsilon_s \tag{8}$$

$$\varepsilon_s = \frac{\varepsilon_L p}{p + P_L} \tag{9}$$

where α is the Biot's coefficient, K is the bulk modulus of shale, σ is the average stress, ε_s is the sorption-induced volumetric strain, ε_L the Langmuir volumetric strain constant representing the volumetric strain at infinite pore pressure. Obviously, the effects of gas sorption, shale deformation, and pore pressure on the permeability of the matrix are included in the model indirectly.

For simplicity, nanopores in shale are considered as straight nanotubes with radius r, length l. The nanopore volume can be defined as:

$$V_p = \pi r^2 l \tag{10}$$

By combining Eqs. (8) and (10), the stress-dependent pore radius can be expressed as

$$r = \frac{r_0}{\sqrt{1 + \frac{\alpha}{\phi K}(\Delta\sigma - \Delta p) - \Delta\varepsilon_s}} \tag{11}$$

where r_0 is the initial radius. Substituting Eq. (11) into Eq. (6) yields stress dependent diffusion coefficient as

$$D = \frac{D_0}{\sqrt{1 + \frac{\alpha}{\phi K}(\Delta\sigma - \Delta p) - \Delta\varepsilon_s}} \tag{12}$$

where D_0 is the initial diffusion coefficient.

Substituting Eq. (11) into Eq. (7) yields the total mass flux that considering the stress influence as

$$J = -\left(\frac{\rho}{8\mu} r_0^2 \frac{1}{1 + \frac{\alpha}{\phi K}(\Delta\sigma - \Delta p) - \Delta\varepsilon_s} + \frac{M}{RT}\frac{2r_0\phi}{3\tau}\sqrt{\frac{8RT}{\pi M\left(1 + \frac{\alpha}{\phi K}(\Delta\sigma - \Delta p) - \Delta\varepsilon_s\right)}} \right)\nabla p \tag{13}$$

The mass transfer between different region can be considered as diffusion through nanopores connecting these two systems. In a pseudo-steady-state, the rate of mass transfer per unit bulk volume is proportional to the pressure difference. Thus, the mass transfer rate can be described as (Fathi and Akkutlu, 2014):

$$Q = aD(\rho - \rho_f) \tag{14}$$

where a is a shape factor, ρ_f is gas density in fracture.

For 2D 3D parallelepiped matrix blocks of lateral dimension, the value of y can be obtained from (Lim and Aziz, 1995):

$$a = \frac{2\pi^2}{L} \tag{15}$$

where L is matrix length.

Combining Eqs. (1), (2), (13) and (14), the gas mass balance equation for shale in micro-scale is:

$$\frac{\partial\left((1-\phi)\rho_s\rho_a\frac{L_a p}{p+L_b} + +\phi p\frac{M}{RT}\right)}{\partial t} - \left(\frac{\rho}{8\mu} r_0^2 \frac{1}{1 + \frac{\alpha}{\phi K}(\Delta\sigma - \Delta p) - \Delta\varepsilon_s} + \frac{M}{RT}\frac{2r_0\phi}{3\tau}\sqrt{\frac{8RT}{\pi M\left(1 + \frac{\alpha}{\phi K}(\Delta\sigma - \Delta p) - \Delta\varepsilon_s\right)}} \right)\nabla p = aD\left(\rho - \rho_f\right) \tag{16}$$

This equation covers all the gas storage states and flows patterns for shale in micro-scale. The mass equations for different materials are controlled by the corresponding parameters.

2.2. Governing equations for mechanical deformation

According to the theory of continuum mechanics, the combination of equilibrium equation with the constitutive equations for the homogeneous, isotropic, and elastic medium derives the Navier-type equation (Wu et al., 2010),

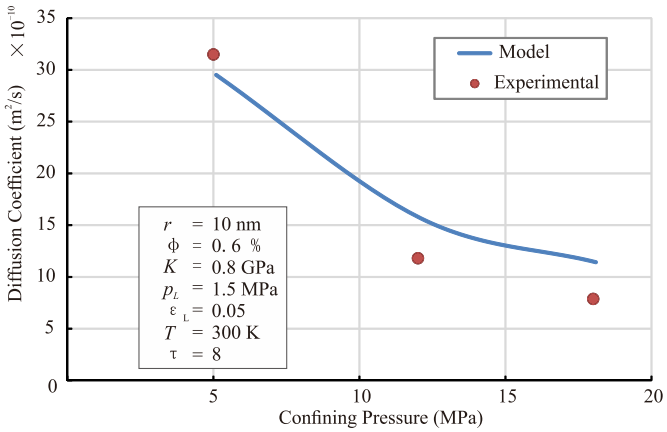

Fig. 2. Comparison of model and experimental results under different confining pressure.

$$Gu_{i,kk} + \frac{G}{1-2\nu}u_{k,ik} - \alpha p_i - K\varepsilon_L\frac{P_L}{(p+P_L)^2}p_i + f_i = 0 \tag{17}$$

where u_i is the component of displacement in the i -direction, G the shear modulus, ν the Poisson's ratio, and f_i the component of body force in the i –direction. The coupling relationship between gas flow and deformation in shale was established based on the diffusion coefficient that is affected by deformation. The gas pressure distribution also has a large impact on effective stress according to the principle of effective stress.

3. Verification

A set of experimental data has been selected for evaluation of quality of diffusion coefficient model that changes with effective stress. The samples used for measurement was collected from Permian Shanxi formation in the southern Qinshui basin and eastern Ordos basin (Meng and Li, 2016). The diffusion coefficient was calculated based on the Fick's second law. The first experiment was performed under different confining stress but at the same temperature and gas pressure. As can be seen in Fig. 2, the measured diffusion coefficient decreases with the increase of confining pressure. The model results calculated by Eq. (11) are plotted with a blue line. It is evident from Fig. 1 that the model prediction is consistent with the experiment data, indicating that the model is reliable. With the increase of confining pressure, effective stress increases due to the constant gas pressure. The compaction of the sample leads to the decrease of pores space and the decrease of the diffusion coefficient. Diffusion coefficient was also measured under conditions of different gas pressure, but with same temperature and confining pressure. From Fig. 3, it can be seen that the diffusion coefficient is enhanced with the increasing gas pressure. Due to the constant confining pressure, effective stress decreases when gas is injected in to sample. The pores radius enlarges with an increases of injected gas pressure, which enhances the diffusion coefficient. It could be concluded that the stress-dependent diffusion coefficient can be predicted consistently by the proposed model.

4. Numerical simulation

Based on current understanding of shale pore structure, fractures including natural fractures and hydraulic fractures provide the flow pathway to produce gas from shale. The organic matter is considered to be isolated packets scattered within the inorganic matter. As can be observed in Fig. 1, almost all the nanopores are only located inside the kerogen. However, there is also a small part of pores in kerogen besides the recognizable nanopores in image segmentation. Hence, free gas can be stored in nanopore space, kerogen and void space in the matrix

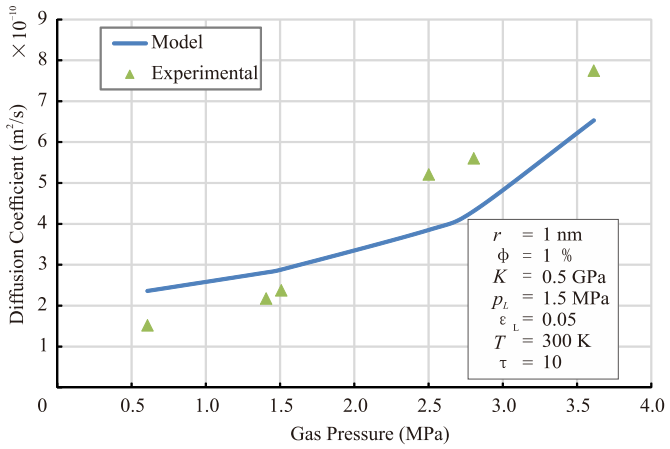

Fig. 3. Comparison of model and experimental results under different gas pressure.

(Javadpour, 2009). Note that adsorbed gas in nanopore is neglected due to the large free space of nanopore in this paper. The form of adsorbed gas only can be stored inside kerogen. During gas production, gas is first produced from a natural and hydraulic fracture network. Then, gas is released from inorganic material to the fracture driven by diffusion due to the density gradient. The gas, in turn, is fed from kerogen into the matrix through gas desorption. Because the kerogen can be connected to fractures through nanopores, the gas desorbed into nanopores from kerogen feeds the fractures through a diffusion process. Total mass transports from nanopore and matrix contributes the source of gas production (Curtis et al., 2011; Liu et al., 2016; Sun et al., 2015; Yan et al., 2013).

A micro-scale geometry model of shale matrix was built based on the pore structure of the SEM image. The model has a length of 2.581 μm, a 1.857 μm width as presented in Fig. 4. The pore distribution, shape, and content are explicitly simulated. The computational domain of this model was divided into three zones with different physical parameters. The gas pressure and deformation are continuous on the zone boundaries. The desorbed gas from kerogen flows into matrix and nanopore. Then the combined flux diffuses into fractures. Considering fracture is the main transfer pathway for gas from the matrix to well-bore, the gas production from the matrix is assumed as the gas flow to fracture. Sink-source term of mass balance equation is defined as Eq. (13). Mass balance for gas follows Eq. (15). Equilibrium equation for mechanical deformation is Eq. (16). The derived governing equations for the gas flow are a set of non-linear partial differential equations (PDE) with the second order in space and the first order in time. All the equations were implemented and solved numerically using the COMSOL Multiphysics simulation software. The different flow mechanisms for three media are achieved by assigning corresponding parameters to each zone. It presents the media properties in Table 1. The boundary condition is assumed to be constant confining pressure of 50 MPa. The reservoir gas pressure is 20 MPa and fracture gas pressure is 5 MPa. The parameters related to each medium are listed in Table 1 that are based on measurements and estimates (Curtis, 2002; Jarvie, 2012; Kumar et al., 2012; Yan et al., 2016).

4.1. Evolution of diffusion coefficient

It shows the pressure distribution of gas and volumetric strain distribution in Fig. 5. This figure indicates that gas pressure in kerogen significantly varies after 10 days. However, the gas pressure in the matrix zone is much greater due to the low permeability. Therefore, there is a high difference in the adjacent zone. Shrinkage strain occurs when gas pressure decreases in a nanopore at first. Then the gas desorption from kerogen lead to shrink of kerogen. The nanopore space decreases significantly. It can be seen that the strain of the matrix is extremely small because of the high bulk modulus.

The pore diameter decreases with the decreasing kerogen volume. It causes the decrease of diffusion coefficient based on the proposed model. The evolution of the diffusion coefficient for each medium are plotted in Fig. 6. Three curves represent the ratio of diffusion coefficient for nanopore, kerogen, and matrix respectively. The measured points in each medium are also marked in the figure. It is evident that the diffusion coefficients decrease in all three media. As mentioned above, the nanopore space has a sharp decrease after the decrease of gas pressure because of the resulting increase in the effective stress. The diffusion coefficient for nanopore drops rapidly at the beginning. Then it keeps steady at the following stage when effective stress unchanged. The diffusion coefficient for kerogen decreases over time. The trend is smoother because of the initial low diffusion coefficient. The diffusion coefficients for nanopore and kerogen reduce to one-third of the initial value after 20 days. The change of diffusion coefficient for the matrix is quite trivial that is negligible. The result demonstrates that diffusion coefficient decreases with the increase of effective stress after gas production. The reduction of the diffusion coefficient relates to its bulk modulus.

Fig. 7 illustrates the diffusion coefficient distribution around nanopore. The location of the cut line is marked in Fig. 5. It crosses the center of one nanopore. It can be seen that the diffusion coefficient changes not only over time but also changes with space location. Because of the pressure drop in a nanopore, the diffusion coefficient is lower in nanopore than that in kerogen in an early stage. It indicates that the gas is transferred to fracture through nanopore mainly. It confirms that diffusion in kerogen does significantly affect production as a result of gas mass release from kerogen to flow pathway. After the

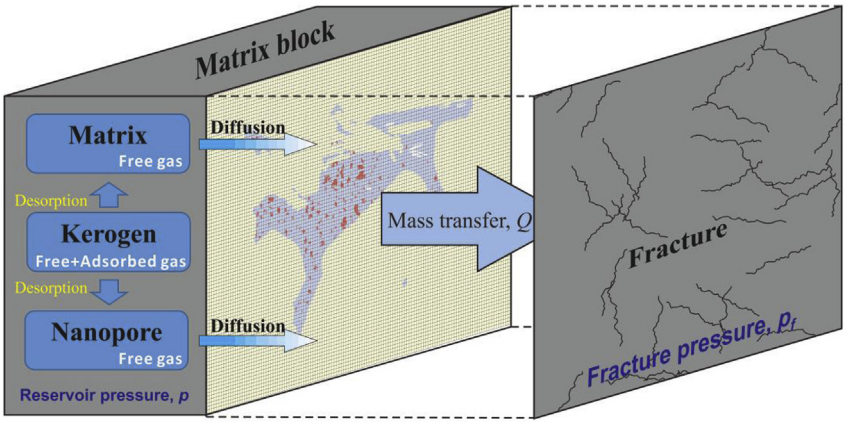

Fig. 4. Schematic of representation of the shale gas transfer system.

Table 1
Parameters for micro-scale geometry model.

Property	Organic matter		Matrix (Yellow Zone)
	Nanopore (Red Zone)	Kerogen (Bule Zone)	
Porosity, ϕ (Total is 6%)	95%	18%	3%
Shale density, ρ_s	0	1350 kg/m^3	2600
Langmuir volume constant, L_a	0	0.017 m^3/kg	0
Langmuir pressure, L_b	0	10 MPa	0
Langmuir volumetric strain constant, ε_L	0	0.02	0
Gas viscosity, u	1.84×10^{-5} Pa s	1.84×10^{-5} Pa s	1.84×10^{-5} Pa s
Initial pore radius, r_0	30 nm	3 nm	0.3 nm
Bulk modulus, K	0 GPa	5 GPa	30 GPa
Poisson's ratio, ν	0.25	0.25	0.25
Initial diffusion coefficient, D_0	7.56×10^{-8} m^2/s	7.56×10^{-9} m^2/s	7.56×10^{-10} m^2/s
Volume percentage	0.97%	13.39%	85.64%
Weight percentage	0	8%	92%

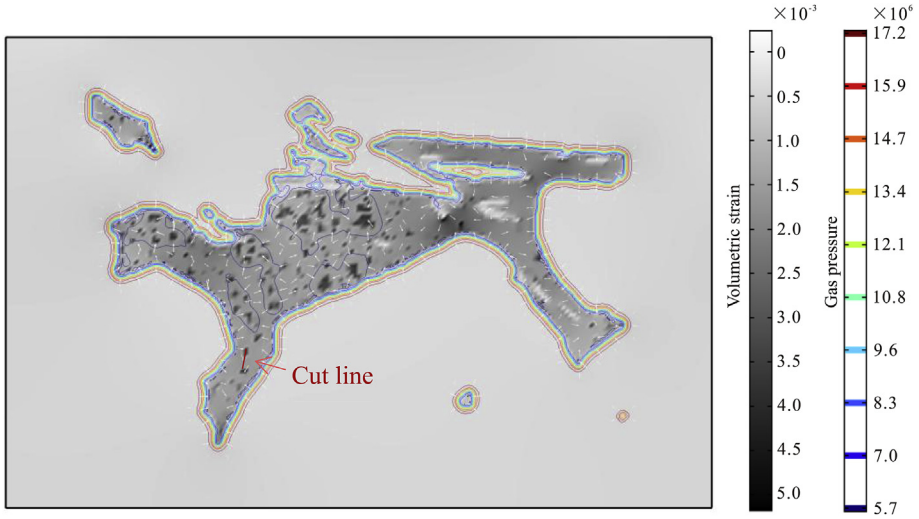

Fig. 5. Distribution of gas pressure and volumetric strain after 10 days.

gas pressure drops in nanopore, the adsorbed gas in kerogen releases into nanopore as free gas. Then it results in the decrease of diffusion coefficient in kerogen. After 5 days, the difference of diffusion coefficient between nanopore and kerogen is reduced. The simulation results confirm that the variation in the diffusion coefficient is both time-dependent and space-dependent.

4.2. Comparison with dual porosity model

A dual porosity model with homogeneous matrix and fracture grids is built to compare with micro-scale geometry model. All property parameters and boundaries are selected to equalize the condition of micro-scale geometry model. The mass balance equations are formed on

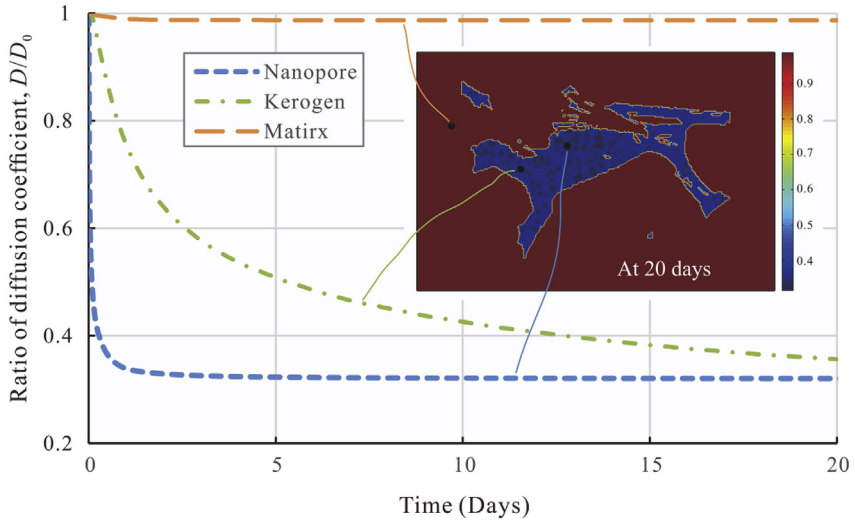

Fig. 6. Evolution of diffusion coefficient for each medium versus time.

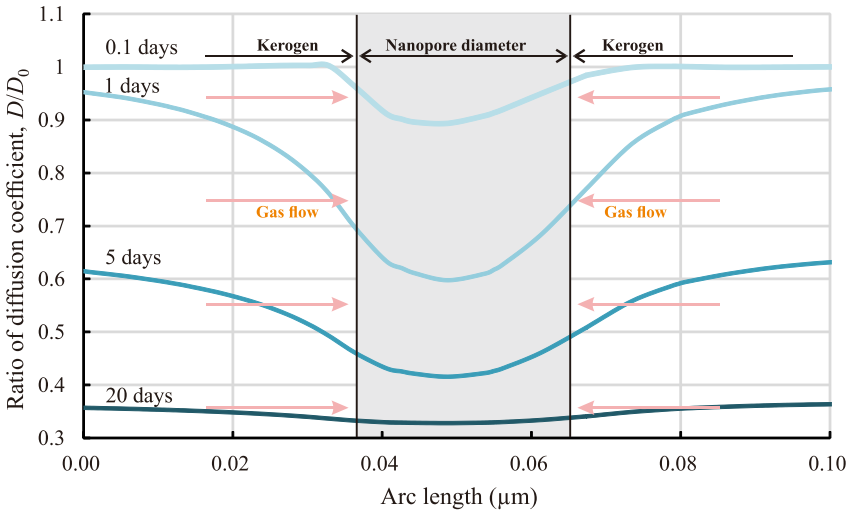

Fig. 7. Diffusion coefficient distribution alone cut line.

Table 2
Parameters for dual porosity model.

Parameters	Kerogen	Matrix
Porosity	18%	19.18%
Langmuir volume constant	0.017 m^3/kg	0
Langmuir pressure	10 MPa	0
Langmuir volumetric strain constant	0.02	0
Gas viscosity	1.84×10^{-5} Pa s	1.84×10^{-5} Pa s
Initial pore radius	3 nm	0.3 nm
Bulk modulus	5 GPa	30 GPa
Initial diffusion coefficient	7.56×10^{-9} m^2/s	7.56×10^{-10} m^2/s
Size	0.96 μm × 0.64 μm	0.96 μm × 0.64 μm
Weight percentage	8%	92%

the basis of Eq. (16), and governing equations for mechanical deformation follows Eq. (17). Table 2 lists the parameters related to dual porosity model.

Fig. 8 shows the simulation results of cumulative gas and average daily flow rate flowing into fracture with micro-scale geometry model and dual porosity model. A significant different between two models can be seen. With the same gas in place, the production rate with micro-scale geometry model is obviously higher than that of dual porosity model in the first 2 days. As the production continuing, the production rate with dual porosity model decreases slower and exceeds the production rate with micro-scale geometry model. The deviation is obvious for accumulated production curves along the whole production history. The accumulated production from shale matrix block to fracture of

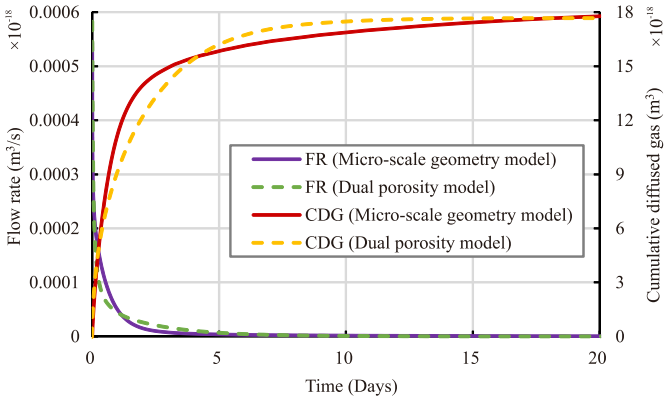

Fig. 8. Comparison between micro-scale geometry model and dual porosity model. FR represents the flow rate. CDG represents cumulative diffused gas.

micro-scale geometry model is great than that of dual porosity model in first 5 days. Then the trend of production rate is lower. The cumulative production is almost the same for the two models at the last stage. This conflict indicates the dual porosity model fails to capture the storage and transport mechanisms in micro-scale.

4.3. The contributions of each medium for gas production

In order to evaluate the impact of the variation of the diffusion coefficient on gas production, a comparison result of cumulative production with different diffusion coefficients is plotted in Fig. 9. The governing gas diffusion over domains of three media is calculated through the integral method. The first case is that the diffusion coefficient keeps constant in the simulation (dash line). For comparison purpose, the change of diffusion coefficient is impacted by effective stress in the other case (solid line). As discussed above, the diffusion coefficient decreases over time during gas production for each medium. The results show that reduction of diffusion coefficient can significantly cut down the adsorbed gas production in kerogen. It is about 8.3 percent less induced by a decrease of the diffusion coefficient. However, it has a minor impact on gas production in matrix and nanopore. For the matrix, it is because its diffusion coefficient is nearly unchanged. The gas production from nanopore is smaller when the change of the diffusion coefficient is considered, but the difference is negligible. Even the diffusion coefficient drops sharply after production, its impact on gas flow in nanopore is minor due to the high initial diffusion coefficient. The amount of gas production can be overestimated if the effect of diffusion coefficient evolution is disregarded.

Different transport mechanics controls the gas flow in the matrix, nanopore, and kerogen separately. Thus the recovery rate for three media is different. Fig. 10 shows the recovery rate of gas in the matrix, nanopore and kerogen during gas production. It can be seen that the recovery rates of free gas in matrix and nanopore are closed to 75% after 20 days. However, the quantity of adsorbed gas in kerogen released to fracture is only 22%. And 40% of the total gas in shale block is produced at last. The results indicate that free gas has a significant contribution to total production. It suggests that a large proportion of adsorbed gas is unable to liberate that results in the low recovery rate of shale gas.

The gas from different domains contributes to the total gas flow as shown in Fig. 4. The flow rate is controlled by the initial recoverable reserve and production capability. As a consequence, the individual contribution of gas from three media to cumulative production is remarkably different at different stages of gas production. Fig. 11 shows the average daily flow rate and recovery rate during gas production. It

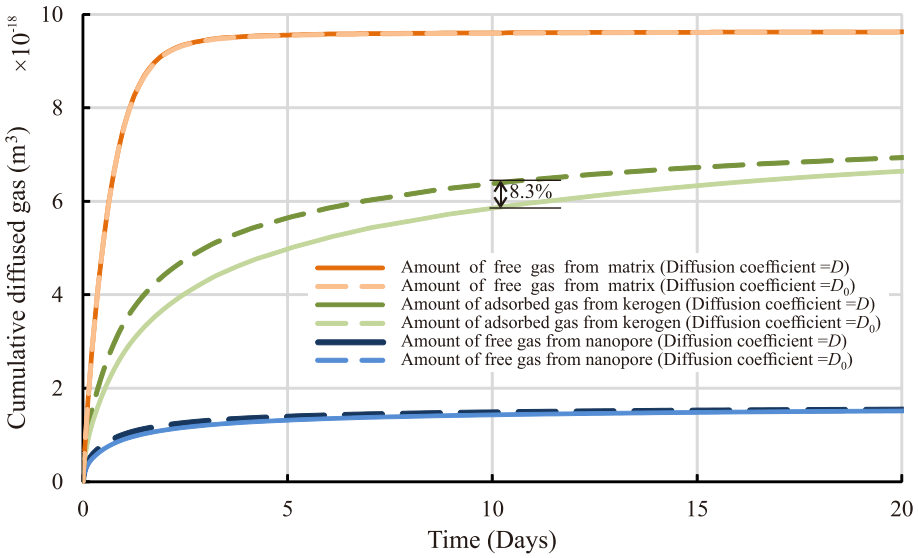

Fig. 9. Effect of diffusion coefficient evolution on cumulative diffused gas for each medium.

clearly shows that the flow rate declines dramatically in the first 2 days and gradually becomes stable later. It can be observed that the cumulative production reaches to 30% after 3 days. Then it increases to 38% in the last 17 days. The portion of free gas from nanopore is about 8.3% and almost unchanged in the whole procedure. The gas in free state from the matrix contributes 60% of the recovery. It can be observed that the portion of gas from the matrix reduces to 54% at last. On the contrary, the contribution of gas from kerogen is growing. It implies that free gas flows into a fracture in response to pressure drop. The adsorbed gas can be desorbed and diffused from kerogen to fracture after a critical production pressure reaches. It could be concluded that the later stage of gas production is depended on the supply of adsorbed gas in kerogen.

5. Conclusion

The following conclusions can be drawn based on the results of this study:

(1) This research proposed a simulation approach to model the complex geometry of nanopore structures in the shale formation. Based on SEM image segmentation of shale matrix, the geometry of three compositions (nanopore, kerogen, and matrix) are explicitly simulated. The pore distribution, shape, content of shale in micro-scale are properly characterized. Mass storage and transport mechanisms in the micro-scale are precisely described by balance equations. And geo-mechanical properties are established based on the theory of continuum mechanics. The comparison of the micro-scale model with the conventional dual-porosity model demonstrates that a dual porosity model fails to capture the storage and transport mechanisms in micro-scale.

(2) The interactions between gas and pore structure in such heterogeneous property have an impact on the diffusion coefficient. The coupling between stress and diffusion coefficient is considered in the model. During depressurization development in shale gas reservoirs, the effective stress increases, resulting in decreasing of diffusion coefficient due to the decrease of pore radius. The diffusion coefficient for nanopore drops rapidly at the beginning then reduces to one-third at the final stage. The reduction of the diffusion coefficient can significantly cut down the adsorbed gas production in kerogen. The diffusion coefficient for kerogen decreases over time with smoother tendency. The change of diffusion

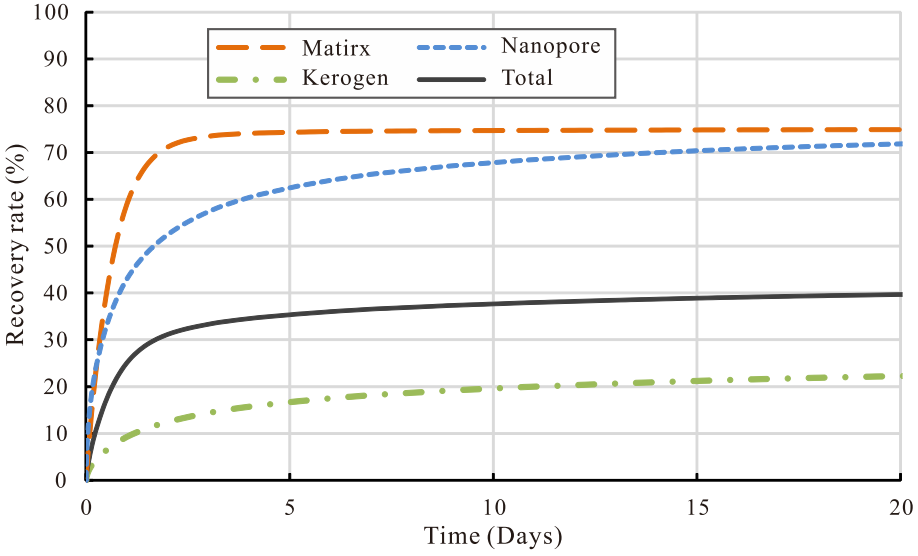

Fig. 10. The recovery rate for each medium during gas production.

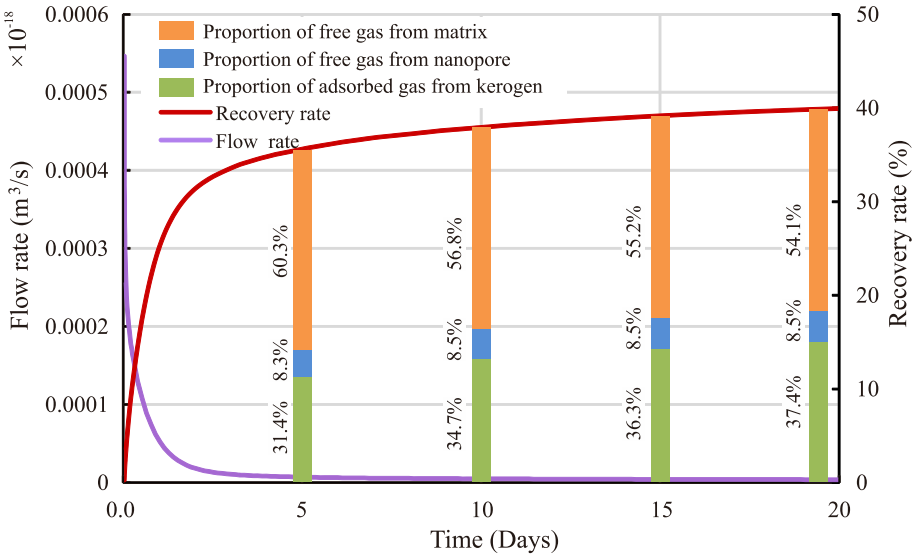

Fig. 11. The contributions of each medium for gas production.

coefficient for the matrix is quite small that is negligible. The variation in the diffusion coefficient is both time-dependent and space-dependent.

(3) The recovery rates of free gas in matrix and nanopore are closed to 75%. Free gas has a significant contribution to total production. A large proportion of adsorbed gas is unable to liberate that result in the low recovery rate of shale gas. The adsorbed gas can be desorbed and diffused from kerogen to fracture after a critical production pressure reaches. The later stage of gas production is depended on the supply of adsorbed gas in kerogen.

Acknowledgments

This work was supported by the Program for Changjiang Scholars and Innovative Research Team in University (Grant no. IRT_17R103), the Fundamental Research Funds for the Central Universities (Grant no. 2018CXTD01), the Priority Academic Program Development of Jiangsu Higher Education Institutions, and the National Natural Science Foundation of China (51504235; 51474204; 51774277). These sources of support are gratefully acknowledged.

Appendix A. Supplementary data

Supplementary data to this article can be found online at https://doi.org/10.1016/j.petrol.2019.01.039.

References

Akkutlu, I.Y., Fathi, E., 2012. Multiscale gas transport in shales with local kerogen heterogeneities. SPE J. 17 (4), 1002–1011.
Al-Owihan, H., Al-Wadi, M., Thakur, S., Behbehani, S., Al-Jabari, N., Dernaika, M., Koronfol, S., 2014. Advanced rock characterization by dual energy CT imaging: a novel method in complex reservoir evaluation. In: International Petroleum Technology Conference.
Alahmadi, H.A., 2010. A Triple-Porosity Model for Fractured Horizontal Wells. Doctoral Dissertation. Texas A&M University.
Ali Beskok, G.E.K., 1999. Report: a model for flows in channels, pipes, and ducts at micro and nano scales. Microscale Thermophys. Eng. 3 (1), 43–77.
Amabeoku, M.O., Al-Ghamdi, T.M., Mu, Y., Toelke, J., 2013. Evaluation and application of digital rock physics (DRP) for special core analysis in carbonate formations. In: International Petroleum Technology Conference.
Baradez, M.O., Mcguckin, C.P., Forraz, N., Pettengell, R., Hoppe, A., 2004. Robust and automated unimodal histogram thresholding and potential applications. Pattern Recogn. 37 (6), 1131–1148.
Barenblatt, G.I., Zheltov, I.P., Kochina, I.N., 1960. Basic concepts in the theory of seepage of homogeneous liquids in fissured rocks [strata]. J. Appl. Math. Mech. 24 (5), 1286–1303.
Bernard, S., Wirth, R., Schreiber, A., Schulz, H.M., Horsfield, B., 2012. Formation of nanoporous pyrobitumen residues during maturation of the barnett shale (fort worth basin). Int. J. Coal Geol. 103 (23), 3–11.
Bird, R.B., Stewart, W.E., Lightfoot, E.N., 2007. Transport Phenomena, second ed. John Wiley & Sons, Inc., Hoboken, NJ.
Bonnie, J.H.M., Fens, T.W., 1992. Porosity and permeability from SEM based image analysis of core material. In: SPE Latin America Petroleum Engineering Conference.
Bustin, R.M., Bustin, A.M.M., Cui, A., Ross, D., Pathi, V.M., 2008. Impact of shale properties on pore structure and storage characteristics. In: SPE Shale Gas Production Conference.
Cipolla, C.L., Lolon, E.P., Erdle, J.C., Rubin, B., 2010. Reservoir modeling in shale-gas reservoirs. Reserv. Eval. Eng. 13 (4), 848–854.
Civan, F., 2010. Effective correlation of apparent gas permeability in tight porous media. Transport Porous Media 82 (2), 375–384.
Clarkson, C.R., Ertekin, T., 2010. A new model for shale gas matrix flow using the dynamic-slippage concept. In: AAPG Hedberg Conference.
Curtis, J.B., 2002. Fractured shale-gas systems. AAPG Bull. 86 (11), 1921–1938.
Curtis, M.E., Ambrose, R.J., Sondergeld, C.H., Rai, C.S., 2011. Investigation of the relationship between organic porosity and thermal maturity in the marcellus shale. In: SPE North American Unconventiongal Gas Conference.
David, C., Wong, T.F., Zhu, W., Zhang, J., 1994. Laboratory measurement of compaction-induced permeability change in porous rocks: implications for the generation and maintenance of pore pressure excess in the crust. Pure Appl. Geophys. 143 (1–3), 425–456.
Dong, J.J., Hsu, J.Y., Wu, W.J., Shimamoto, T., Hung, J.H., Yeh, E.C., Wu, Y.H., Sone, H., 2010. Stress-dependence of the permeability and porosity of sandstone and shale from TCDP Hole-A. Int. J. Rock. Mech. Min. 47 (7), 1141–1157.
Durucan, S., Edwards, J.S., 1986. The effects of stress and fracturing on permeability of coal. Min. Sci. Technol. 3 (3), 205–216.
Ertekin, King, G.R., Schwerer, F.C., 1986. Dynamic gas slippage: a unique dual-mechanism approach to the flow of gas in tight formations. SPE Form. Eval. 1 (1), 43–52.
Farah, N., 2017. Flow Modelling in Low Permeability Unconventional Reservoirs.
Fathi, E., Akkutlu, I.Y., 2014. Multi-component gas transport and adsorption effects during CO_2 injection and enhanced shale gas recovery. Int. J. Coal Geol. 123 (2), 52–61.
Gallagher Jr., N.C., Wise, G.L., 1981. A theoretical analysis of the properties of median filters. IEEE Trans. Acoust. Speech Signal Process 29 (6), 1136–1141.
Hadjiconstantinou, N.G., 2006. The limits of Navier-Stokes theory and kinetic extensions for describing small scale gaseous hydrodynamics. Phys. Fluids 18 (11), 111301–111319.
Harpalani, S., Schraufnagel, R.A., 1990. Shrinkage of coal matrix with release of gas and its impact on permeability of coal. Fuel 69 (5), 551–556.
Hashmy, K., Abueita, S., Barnett, C., Jonkers, J., 2011. Log-based identification of sweet spots for effective fracs in shale reservoirs. In: SPE Canadian Unconventional Resources Conference.
He, S., Jiang, Y., Conrad, J.C., Qin, G., 2015. Molecular simulation of natural gas transport and storage in shale rocks with heterogeneous nano-pore structures. J. Petrol. Sci. Eng. 133, 401–409.
Hosking, L.J., Thomas, H.R., Sedighi, M., 2017. A dual porosity model of high-pressure gas flow for geoenergy applicat. Can. Geotech. J.(6).
Janiga, D., Czarnota, R., Stopa, J., Wojnarowski, P., Kosowski, P., 2017. Performance of nature inspired optimization algorithms for polymer enhanced oil recovery process. J. Petrol. Sci. Eng. 154, 354–366.
Janiga, D., Czarnota, R., Stopa, J., Wojnarowski, P., 2018. Huff and puff process optimization in micro scale by coupling laboratory experiment and numerical simulation. Fuel 224, 289–301.
Jarvie, D.M., 2012. Shale resource systems for oil and gas: Part 1—shale-gas resource

systems. AAPG Memoir. 97, 89–119.
Javadpour, F., 2009. Nanopores and apparent permeability of gas flow in mudrocks (shales and siltstone). J. Can. Petrol. Technol. 48 (8), 16–21.
Karniadakis, G.E., Beskok, A., Aluru, N.R., 2004. MicroFlows and nanoflows - fundamentals and simulation. Interdis. Appl. Math. Seri. 66–74.
Kumar, V., Curtis, M.E., Gupta, N., Sondergeld, C.H., Rai, C.S., 2012. Estimation of elastic properties of organic matter in woodford shale through nanoindentation measurements. In: SPE Canadian Unconventional Resources Conference.
Langmuir, I., 1918. The adsorption of gases on plane surfaces of glass, mica and platinum. J. Chem. Phys. 40 (9), 1361–1403.
Lim, K.T., Aziz, K., 1995. Matrix-fracture transfer shape factors for dual-porosity simulators. J. Petrol. Sci. Eng. 13 (3–4), 169–178.
Liu, J.S., Chen, Z.W., Elsworth, D., Qu, H.Y., Chen, D., 2011. Interactions of multiple processes during CBM extraction: a critical review. Int. J. Coal Geol. 87 (3), 175–189.
Liu, H.H., Ranjith, P.G., Georgi, D.T., Lai, B.T., 2016. Some key technical issues in modelling of gas transport process in shales: a review. Geomech. Geophys. Geo-Energy . Geo-Res. 2 (4), 231–243.
Loucks, R.G., Reed, R.M., Ruppel, S.C., Hammes, U., 2015. Spectrum of pore types and networks in mudrocks and a descriptive classification for matrix-related mudrock pores. AAPG Bull. 96 (6), 1071–1098.
Mckernan, R.E., Rutter, E.H., Mecklenburgh, J., Taylor, K.G., Covey-Crump, S.J., 2014. Influence of effective pressure on mudstone matrix permeability: implications for shale gas production. In: SPE European Unconventional Resources Conference.
Mehmani, A., Prodanović, M., Javadpour, F., 2013. Multiscale, Multiphysics network modeling of shale matrix gas flows. Transport Porous Media 99 (2), 377–390.
Mehrabi, M., Javadpour, F., Sepehrnoori, K., 2017. Analytical analysis of gas diffusion into non-circular pores of shale organic matter. J. Fluid Mech. 819 (656).
Meng, Y., Li, Z.P., 2016. Experimental study on diffusion property of methane gas in coal and its influencing factors. Fuel 185, 219–228.
Moghanloo, R.G., Javadpour, F., 2014. Applying method of characteristics to determine pressure distribution in 1D shale-gas samples. SPE J. 19 (3), 361–372.
Palmer, I., 2009. Permeability changes in coal: analytical modeling. Int. J. Coal Geol. 77 (1), 119–126.
Pan, Z.J., Connell, L.D., Camilleri, M., 2010. Laboratory characterisation of coal reservoir permeability for primary and enhanced coalbed methane recovery. Int. J. Coal Geol. 82 (3), 252–261.
Reed, R.M., Loucks, R.G., Jarvie, D.M., 2007. Nanopores in the mississippian barnett shale: distribution morphology, and possible genesis. Gas shales of north America. In: GSA Denver Annual Meeting.
Robertson, E.P., Christiansen, R.L., 2006. A permeability model for coal and other fractured, sorptive-elastic media. SPE J. 13 (3), 314–324.
Rodriguez, R., Crandall, D., Song, X., Verba, C., Soeder, D., 2014. Imaging Techniques for Analyzing Shale Pores and Minerals. NETL Technical Report Series.
Roy, S., Raju, R., Chuang, H.F., Cruden, B.A., 2003. Modeling gas flow through microchannels and nanopores. J. Appl. Phys. 93 (8), 4870–4879.
Shabro, V., Torres-Verdin, C., Javadpour, F., 2011. Numerical simulation of shale-gas production: from pore-scale modeling of slip-flow knudsen diffusion and Langmuir desorption to reservoir modeling of compressible fluid. In: SPE North American Unconventional Gas Conference.
Shi, J.Q., Durucan, S., 2004. Drawdown induced changes in permeability of coalbeds: a new interpretation of the reservoir response to primary recovery. Transport Porous Media 56 (1), 1–16.
Si, L., Li, Z., Yang, Y., 2018. Influence of the pore geometry structure on the evolution of gas permeability. Transport Porous Media 123 (2), 321–339.
Sun, H., Chawathe, A., Hoteit, H., Shi, X., Li, L., 2015. Understanding shale gas flow behavior using numerical simulation. SPE J. 20 (1), 142–154.
Suri, Y., 2011. Predicting petrophysical properties using SEM Image. In: SPE Reservoir Characterisation and Simulation Conference.
Tissot, B.P., Welte, D.H., 1984. Petroleum Formation and Occurrence. Springer-Verlag.
Vandenbroucke, M., Largeau, C., 2007. Kerogen origin, evolution and structure. Org. Geochem. 38 (5) 719-833.
Walls, J., 2012. Shale reservoir properties from digital rock physics. In: SPE Canadian Unconventional Resources Conference.
Wang, P., M, F., Reed, R., 2009. Pore Networks and Fluid Flow in Gas Shales.
Wei, M.Y., Liu, J.S., Feng, X.T., Wang, C.G., Fang, K., Zhou, F.B., Zhang, S.W., Xia, T.Q., 2016a. Quantitative study on coal permeability evolution with consideration of shear dilation. J. Nat. Gas Sci. Eng. 36.
Wei, M.Y., Liu, J.S., Feng, X.T., Wang, C.G., Zhou, F.B., 2016b. Evolution of shale apparent permeability from stress-controlled to displacement-controlled conditions. J. Nat. Gas Sci. Eng. 34, 1453–1460.
Wei, M.Y., Liu, J.S., Elsworth, D., Wang, E.Y., 2018. Triple-porosity modelling for the simulation of multiscale flow mechanisms in shale reservoirs. Geofluids 1–11 6948726.
Wu, Y., Liu, J.S., Elsworth, D., Chen, Z.W., Connell, L., Pan, Z.J., 2010. Dual poroelastic response of coal seam to CO2 injection. Int. J. Greenh. Gas Con. 4 (4), 668–678.
Wua, K., Li, X., Guo, C., Chen, Z., 2015. Adsorbed gas surface diffusion and bulk gas transport in nanopores of shale reservoirs with real gas effect-adsorption-mechanical coupling. In: SPE Reservoir Simulation Symposium, 23-25 February, Houston, Texas, USA, SPE-173201-MS.
Yan, B., Alfi, M., Wang, Y., Killough, J., 2013. A new approach for the simulation of fluid flow in unconventional reservoirs through multiple permeability modeling. In: SPE Annual Technical Conference and Exhibition.
Yan, B., Wang, Y., Killough, J.E., 2016. Beyond dual-porosity modeling for the simulation of complex flow mechanisms in shale reservoirs. Comput. Geosci. 20 (1), 69–91.
Ziarani, A.S., Aguilera, R., 2012. Knudsen's permeability correction for tight porous media. Transport Porous Media 91 (1), 239–260.